

# Electronic states at twist stacking faults in rhombohedral graphite

Xiaoqian Liu,<sup>1</sup> Yifei Guan,<sup>1</sup> and Oleg V. Yazyev<sup>1,\*</sup>

<sup>1</sup>*Institute of Physics, École Polytechnique Fédérale de Lausanne (EPFL), CH-1015 Lausanne, Switzerland*

(Dated: December 24, 2025)

Flat bands in graphitic materials emerged as a platform for realizing tunable correlated physics. As a nodal-line semimetal, rhombohedral graphite features flat drumhead surface states in the vicinity of the Dirac points, which carry a nontrivial topological charge. We present a comprehensive study on rhombohedral graphite with twist stacking faults. Using both the continuum models and the realistic tight-binding models, we show that the twist angle between the graphene layers can tune the interface states at such stacking faults. The evolution of interface states originates from the interplay between the moiré periodicity and Zak phase topology, predicting the occurrence of nearly flat bands throughout the moiré Brillouin zone. We further investigate the disorder-induced layer polarization and tunable Chern number for flat band, and characterize the relationship between the disorder strength and Chern number in twisted rhombohedral graphite.

Twistronics, an approach unique to 2D materials, dramatically alters the band structure and electronic properties through variations in the twist angle [1, 2]. Graphene-like systems exhibit exceptional electronic properties due to their Dirac-like charge carriers and linear energy dispersion near the Fermi level [3]. These properties lead to high carrier mobility and suppressed scattering from long-range disorder [4], making graphene a compelling candidate for electronic applications. Based on the intrinsic properties of graphene, twisted bilayer graphene (TBG) has garnered significant attention because it exhibits a correlated insulating phase [5–8], unconventional superconductivity [8–10], and notable topological features [11–13], which sparked widespread interest from researchers. Recently, ferromagnetism, superconductivity, and correlated insulating phases have been observed in more complex twisted heterostructures, such as twisted double bilayer graphene [14–16], twisted trilayer graphene [17–19] as well as rhombohedral multilayer graphene [20–22]. This indicates that low-energy flat bands that are responsible for the correlated physics in TBG, may also exist in even more complex physical systems eventually extending to the limit of bulk graphite.

Graphite consists of graphene layers arranged in a Bernal stacking configuration in its thermodynamically stable phase. Beyond Bernal stacking, multilayer graphene can also adopt a metastable rhombohedral stacking arrangement [23]. Unlike Bernal-stacked graphene, multilayer rhombohedral graphene exhibits pronounced electronic correlation effects, including unconventional superconductivity [24, 25] and ferromagnetism [21, 26]. Chirality plays an important role in rhombohedral graphene, leading to several possible states with spontaneously broken symmetry in multi-layer rhombohedral graphene [20, 27]. Upon increasing the number of layers, rhombohedral graphite is deemed to be protected by chiral symmetry [28, 29], exhibiting a quantized Zak phase and protected surface states [30–32]. In the limit of the bulk phase,

rhombohedral graphite is a nodal-line semimetal [33–35].

In this Letter, we investigate the topologically protected flat bands in twisted rhombohedral graphite by using the combination of tight-binding and continuum models. We examine rhombohedral graphite in the chiral limit situation and explore how disorder affects the Chern number of the interface flat band in the rhombohedral systems. Twisting introduces moiré periodicity, which modifies the dispersion of the interface bands through the interplay with the Zak phase topology, and this interface band becomes almost entirely flat when approaching the chiral limit. The momentum resolved density of states and the Zak phase pattern at different twist angles in twisted rhombohedral graphite are illustrated. Analysis reveals that the density of states (DOS) in  $\Gamma$  point varies with the twist angle, and the flat bands dominate the moiré Brillouin Zone (mBZ) near the chiral limit. Furthermore, we illustrated the sublattice-polarized flat bands when approaching the chiral limit. In the low-energy effective model, the Chern number of flat bands scales linearly with the layer count [36, 37], but even weak disorder disrupts this scaling since the bandgap exponentially decays with the number of layers. We address disorder effects, showing that the Chern number in twisted rhombohedral graphite eventually converges.

For the tight-binding (TB) model calculations, we adapted the Slater-Koster formalism [38] for calculating the hopping integrals, which describe intralayer  $\pi$  bonds and interlayer  $\sigma$  bonds formed by the  $p_z$  orbitals of carbon atoms. The atomic positions correspond to the relaxed configurations obtained using LAMMPS [39] with the modified Kolmogorov-Crespi potential [40] for interlayer van der Waals interactions, and REBO potential [41] for intralayer interaction.

The continuum model of twisted rhombohedral graphene is built starting from the effective model for the multilayer rhombohedral graphene. We focus on the low-energy states near the  $K$  point, which we refer to as the  $K$  valley, for multilayer rhombohedral graphene, resulting in a  $2n \times 2n$  Hamiltonian whose basis is the

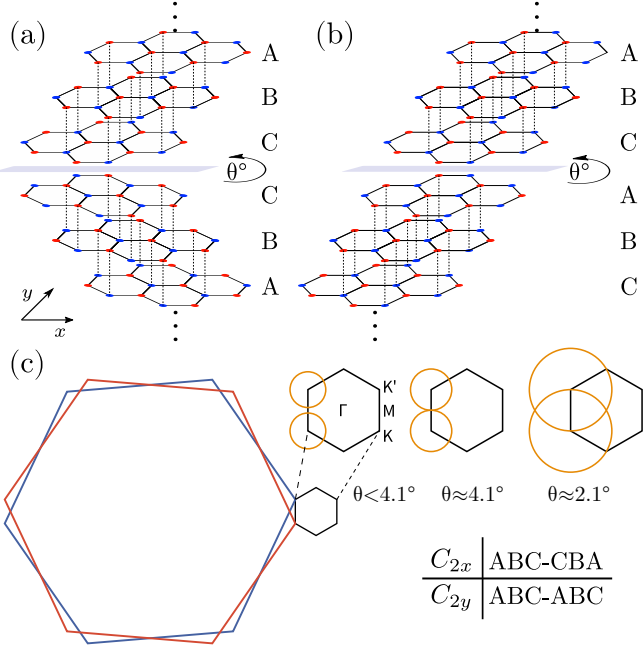


FIG. 1. Twisted stacking faults in rhombohedral graphite with (a) ABC-CBA stacking configuration ( $C_{2x}$  symmetry) and (b) ABC-ABC stacking configuration ( $C_{2y}$  symmetry). (c) Moiré Brillouin Zone of twisted rhombohedral graphite (black hexagons) at different twist angles. Yellow circles delimit the region of  $Z(k_x, k_y) = \pi$ .

layer inner product with the sublattice.

The effect of the twist of the middle graphene layers is described by the twist-induced interlayer coupling  $T_\theta(\mathbf{r})$ , which gives

$$T_\theta(\mathbf{r}) = \sum T_n e^{-i\mathbf{q}_n \cdot \mathbf{r}} \quad (1)$$

with a moiré three-fold star of  $\mathbf{q}_i = 2k_D \sin(\theta/2)$ , equirotated by  $\phi = 2\pi/3$

$$T_n = e^{-i\mathcal{G}_\theta^{(n)} \cdot \mathbf{d}} \hat{\Omega}_\phi^{n-1} \begin{pmatrix} w_{AA} & w_{AB} \\ w_{AB} & w_{AA} \end{pmatrix} \hat{\Omega}_\phi^{1-n} \quad (2)$$

with  $\hat{\Omega}_\phi = \cos \phi \sigma_x - \sin \phi \sigma_y$ . Here,  $\mathcal{G}_\theta^{(0)} = 0$ ,  $\mathcal{G}_\theta^{(1)} = \mathbf{q}_2 - \mathbf{q}_1$ ,  $\mathcal{G}_\theta^{(2)} = \mathbf{q}_3 - \mathbf{q}_1$  are the moiré reciprocal lattice vectors and  $\mathbf{d}$  is the interlayer displacement [1]. The twisted rhombohedral graphite (TRG) Hamiltonian thus reads

$$H(\mathbf{k}) = \begin{pmatrix} \ddots & t^\dagger(\mathbf{k}) & & \\ t(\mathbf{k}) & v_F \mathbf{k} \cdot \sigma & T_\theta^\dagger(\mathbf{r}) & \\ & T_\theta(\mathbf{r}) & v_F \mathbf{k} \cdot \sigma & t^\dagger(\mathbf{k}) \\ & & t(\mathbf{k}) & \ddots \end{pmatrix} \quad (3)$$

More details about the method can be found in I.

Rhombohedral graphite exhibits a distinct stacking sequence that distinguishes it from Bernal-stacked graphite. Unlike Bernal-stacked graphite, where carbon atoms follow the AB stacking sequence, rhombohedral graphite assumes the ABC sequence that breaks inversion symmetry. In turn, this results in the ABC and CBA stacking configurations of different chirality, and one can be transformed into another by a  $60^\circ$  rotation. For comparison, when discussing twist stacking faults, we focus on much smaller twist angles of the order of degrees.

Being a three-dimensional nodal-line semimetal, rhombohedral graphite is characterized by the drumhead surface states [31] originating from the nontrivial Zak phase. Accounting for only the nearest-neighbor coupling between the graphene layers, the system can be modeled as a one-dimensional chain. The Zak phase  $\mathcal{Z}$  is calculated as the integral of the Berry connection over a loop in the mBZ that spans the reciprocal lattice vector,

$$\mathcal{Z}(k_x, k_y) = i \int_{k_z=0}^{2\pi/a_z} \langle u(\mathbf{k}) | \partial_{k_z} | u(\mathbf{k}) \rangle dk_z. \quad (4)$$

where  $a_z$  is the lattice constant in the  $z$ -direction,  $|u(\mathbf{k})\rangle$  are the periodic parts of the Bloch functions at momentum  $\mathbf{k} = (k_x, k_y, k_z)$ . Such topological invariant is quantized in the chiral-symmetric case, i.e. only when the inter-sublattice terms of the Hamiltonian are nonzero. In such a scenario,  $\mathcal{Z} = 0$  and  $\mathcal{Z} = \pi$  are the  $\mathbb{Z}_2$  topological invariant.

In rhombohedral graphite, the nontrivial  $\mathcal{Z} = \pi$  is localized in a narrow region of radius  $\delta_k$  around each Dirac cone of the  $K$  and  $K'$  valley [30], with  $\delta_k \approx \frac{t_\perp}{v_f \hbar} \approx 0.015 \text{ \AA}^{-1}$ , where  $t_\perp$  is the interlayer hopping parameter and  $v_f$  is the Fermi velocity. When a twist is introduced in rhombohedral graphite, the electronic states localized at the twist interface are determined by the interplay between moiré periodicity and  $\delta_k$ . One can anticipate a change in the dispersion and topology of these states when  $\delta_k$  becomes comparable to the mBZ dimensions  $k_D \sin \theta/2$ , where  $k_D$  is the Dirac-point wave vectors in the continuum model and  $\theta$  is the twist angle. Using the TB model to calculate the momentum-resolved DOS, we demonstrate the interface bands and their relationship to the interplay between  $\delta_k$  and the moiré periodicity.

Considering the fact that the surface states of rhombohedral graphite are sublattice polarized [37], the stacking order of the twisted interface determines the coupling regime between the graphite surfaces. Specifically, the change in the valley momenta is controlled by the stacking order of twisted rhombohedral graphite. For the ABC-CBA configuration, as shown in Fig. 1(a), the  $K$  of the bottom layer matched with the  $K'$  in the top layer, and for the ABC-ABC configuration, the  $K$  of the bottom layer should match with the  $K$  in the top layer. Both of the two configurations belong to the  $D_3$  symmetry group, but differ by having the  $C_{2x}$  and

$C_{2y}$  symmetries. The interface in twisted rhombohedral graphite consists of two separate rhombohedral graphite domains; thus, the chirality and sublattice polarization arising from their stacking sequences must be considered when studying interface properties. Due to the reason that the ABC-CBA configuration provides the flatter interface band when approaching the chiral limit, see III, we use ABC-CBA as the default stacking setup below.

The interface of the twisted rhombohedral graphite is described by the Green's function

$$G(E, \mathbf{k}) = [E + i\eta - H(\mathbf{k}) - \Sigma_T(\mathbf{k}) - \Sigma_B(\mathbf{k})]^{-1}, \quad (5)$$

where  $\eta$  is a small energy broadening and  $H$  is the Hamiltonian of the twisted interface, which is essentially the same as TBG.  $\Sigma_T$  and  $\Sigma_B$  are the self-energy terms from the top and bottom semi-infinite rhombohedral graphite. We use the momentum resolved density of states  $\rho(E, \mathbf{k}) = -\frac{1}{\pi} \text{Im}[\text{Tr}G(E, \mathbf{k})]$  to demonstrate the spectrum of interface localized states.

To illustrate how the non-trivial Zak-phase region manifests within the mBZ, we shall focus on the twist angles around  $k_D \sin \theta = \delta_k$  where the  $\mathcal{Z} = \pi$  regions of adjacent moiré valleys are expected to overlap. To be clear, the  $\mathcal{Z} = \pi$  would cancel each other, resulting in the trivial Zak phase  $\mathcal{Z} = 0$  in the overlapped regions. We use two simple cases where the  $\mathcal{Z} = \pi$  pattern evolution to illustrate the interplay. As shown in Figs. 2(a,b), the orange regions represents the  $\mathcal{Z} = \pi$ , and the blank regions represents the  $\mathcal{Z} = 0$  at twist angles  $6.01^\circ$  and  $3.15^\circ$ , respectively. Figs. 2(c,d) show the momentum resolved density of states of the corresponding configurations. The bands near the Fermi level in these two configurations are almost flat. From the Zak phase patterns in Figs. 2(a,b), we can easily associate the flat bands at zero energy with the non-trivial Zak phase.

For twist angles around  $\theta \approx 2.1^\circ$ , as you can see from Fig. 3, only the non-trivial Zak phase ( $\mathcal{Z} = \pi$ ) from the mBZ significantly contributes, simplifying the description of the zero-mode interface states. However, at smaller twist angles, the Zak phase patterns become very complex, respectively resulting in complex dispersion of the interface bands. In such cases, the trigonal warping orientation that is affected by the stacking order can not be ignored. To present the situation at the small twist angle and chiral limit, the evolution of the DOS at  $\Gamma$  would be adopted.

Figure 3 shows the evolution of the DOS of the interface states at the  $\Gamma$  point as a function of twist angle. A pronounced change in the DOS occurs around  $\theta = 2.6^\circ$ , corresponding to the angle, at which the Zak phase in momentum space takes the value of  $\pi$ , reaching the  $\Gamma$  point. At this critical angle, the tight-binding calculation reveals interface bands with finite dispersion extending up to 20 meV. A consistent feature is also observed in the DOS evolution shown in Fig. S1. This energy scale

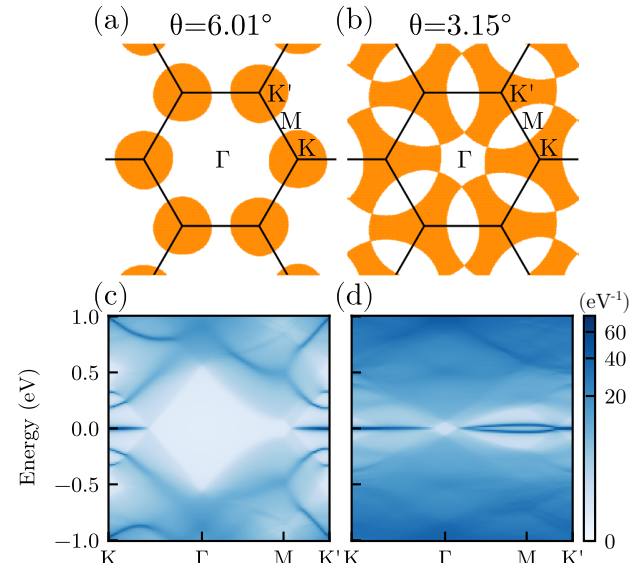


FIG. 2. Maps of the Zak phase of rhombohedral graphite for moiré periodicities that correspond to twist angle (a)  $\theta = 6.01^\circ$  and (b)  $\theta = 3.15^\circ$  showing the regions of  $\mathcal{Z} = \pi$  in orange. Momentum resolved DOS of twisted rhombohedral graphite at (c)  $\theta = 6.01^\circ$  and (d)  $\theta = 3.15^\circ$  calculated using the TB model along the  $k$ -point path  $K - \Gamma - M - K'$ .

can be contrasted with a typical interaction scale [5, 42], where interaction effects are expected to dominate.

Fig 3(a) shows the tight-binding result. The discrete observed in Fig. 3(a) arises from the discrete sampling of twist angles. Figs 3(b) and (c) are the two sublattice continuum model results, which are used to clarify the difference in the chiral limit. Fig. 3(b) shows the finite dispersion with  $w_{AA} = 20$  meV, while Fig. 3(c) shows the chiral limit result revealing a perfectly flat band at the Fermi level. Tight-binding calculation captures interactions beyond nearest neighbors, so the AA coupling would not be zero. As discussed above, the overlap between  $\mathcal{Z} = \pi$  causes the band dispersion, but  $\mathcal{Z} = \pi$  itself is the origin of the interface flat bands. So, once the non-trivial Zak phase extends across the mBZ, the corresponding flat band also emerges throughout the entire zone.

To provide a deeper understanding of the electronic properties of the stacking faults in rhombohedral graphite, the Berry phase physics of the interface bands should be taken into account. While the interface bands are generally not separated from other bands, we retrieve the Berry curvature and valley Chern number by taking the long-sequence limit of twisted rhombohedral multilayer graphene [36, 43]. We model the twisted rhombohedral graphite by coupling  $(M-1)$ -layer graphite to the top and bottom layers of TBG. The chirally stacked  $(M-1)$ -layer graphite is described by

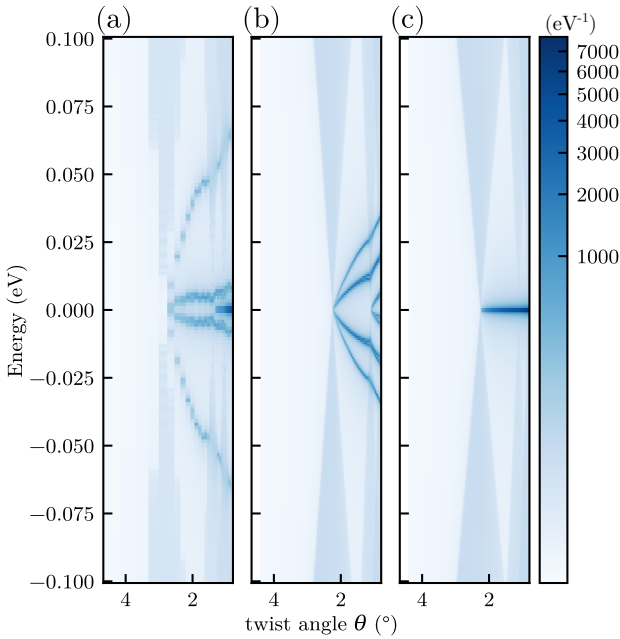


FIG. 3. Evolution of the DOS of rhombohedral graphite (semi-infinite) interface states at  $\Gamma$  point versus twist angles, the twist angle from  $4.41^\circ$  to  $0.8^\circ$ ; (a) Tight-binding model result; (b) continuum model result,  $w_{AA} = 20$  meV; (c) continuum model result, chiral limit,  $w_{AA} = 0$  meV.

the degenerate state perturbation Hamiltonian [44]:

$$H_{M-1} = -t_\perp \begin{pmatrix} 0 & \nu^{M-1} \\ (\nu^\dagger)^{M-1} & 0 \end{pmatrix}, \quad (6)$$

where  $\nu = \hbar v_f(k_x + ik_y)/t_\perp$  represents the effective coupling between the two interface layers of rhombohedral graphene. In such a setup, there exists a set of flat bands with valley Chern numbers  $\pm 2(M-1)$  in the chiral limit, as shown in Fig. 4. The valley Chern bands are equally localized on the twist interface and the outermost layers of graphite.

The chiral models predict a valley Chern number increasing with  $M$ , and this dependence is preserved upon continuing the perturbation series [45]. Here, we can ask a question: will the interface states and the surface states remain coherent if  $M \rightarrow \infty$ ? In ideal cases, yes, the coherence length tends to infinity as the temperature approaches absolute zero  $\xi(T) \approx \frac{\hbar}{\sqrt{2m k_B T}}$ , because there are no thermal disruption to phase coherence. However, in real systems, disorder and quantum fluctuations would limit the coherence length, preventing it from becoming truly infinite. We show below that upon adding non-chiral terms, the interface bands converge to a finite Chern number even in the limit  $M \rightarrow \infty$ .

The non-chiral terms are just the finite AA-sublattice coupling  $w_{AA}$  between the interface TBG layers. By adding this non-chiral term, we can split the interface

state and surface state. As shown in Fig. 4(a), a finite  $w_{AA}$  significantly modifies the interface-layer spectral weight to the interface band and surface band, causing strong layer polarization. As shown in Fig. 4(a), we focus on the states localized at the interface, finding that such bands always carry  $C = \pm 1$  despite the total valley Chern number for interface and surface flat bands  $\pm 2(M-1)$ .

Moreover, in the chiral limit, all the Chern bands distribute equally between the interface and surfaces. Such a delocalization also prevents the Chern number from diverging: the topological number will be constrained by the interlayer coherent length in real systems.

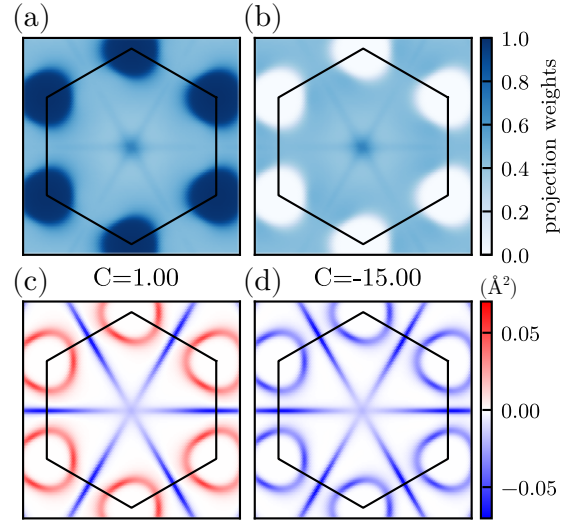


FIG. 4. Spectral weight of the (a) interface and (b) surface bands on the interface layers calculated for the 8+8-layer ABC-CBA configuration. (c,d) Berry curvature maps of the respective bands.

To quantitatively investigate these effects, we perform ensemble averaging over independent configurations to analyze how varying disorder strength affects the total Chern number of flat bands. We add symmetric intervalley coupling  $V = V^\dagger$  as the random scattering between different plane waves to simulate the effect of disorder. In the presence of on-site disorder potentials  $V_i(r_i)$ , the intervalley scattering between moiré valleys  $\mathbf{K}_{1,2}$  writes

$$V_{\chi\bar{\chi}}^{\mathbf{K}_1\mathbf{K}_2} = \sum_{\mathbf{r}} \langle \psi_{\chi,\mathbf{K}_1}(\mathbf{r}) | V(\mathbf{r}) | \psi_{\bar{\chi},\mathbf{K}_2}(\mathbf{r}) \rangle \quad (7)$$

where  $\psi = e^{i\mathbf{K}\cdot\mathbf{r}}$  are the plane-wave basis with  $\mathbf{K}_i = \mathbf{K}_\pm + a_1\mathbf{G}_1 + a_2\mathbf{G}_2$  the indexes of moiré valleys, and  $\chi$  identifies the sublattice.  $V(\mathbf{r}) = \sum_i V_i \delta(\mathbf{r}_i)$  contains the  $\delta$ -function scatterings at positions  $r_i$ . Here, we generate the random scattering disorder sequence with

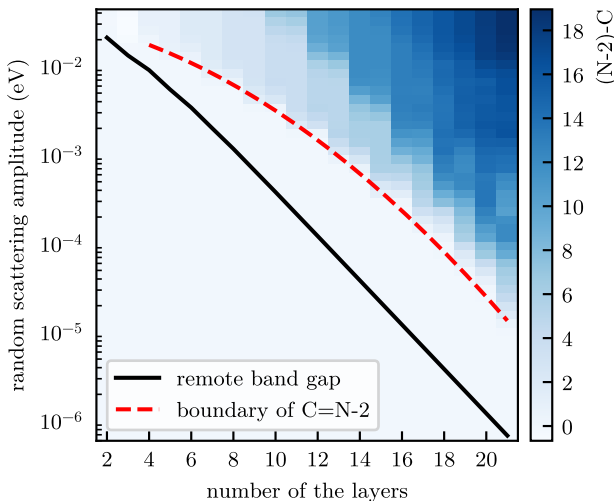


FIG. 5. The evolution of total Chern number of the flat bands with the number of layers and the random scattering disorder amplitude. The black line is the remote band gap strength, the color represents the difference between Chern number and its theoretical value  $N - 2$  [36] to make the evolution clear, where  $N$  is the number of the layers. The random scattering disorder disturbs the linear relation between the number of layers and the total Chern number. The upper limit of 40 meV is critical because the flat band topology for twisted bilayer graphene essentially fails at this disorder strength [46]. The weak disorder that is smaller than the remote band gap will not affect the Chern number of the flat band at all. Additionally, the intervalley scattering could mix the Chern number from different bands. This could eventually cause the total Chern number to vanish. By adding the random scattering disorder and taking the statistical average of the total Chern number sequence, we conclude that the Chern number decreases with increasing the disorder amplitude.

a uniform distribution to calculate the statistical average Chern number and evaluate how the total Chern number would change with the disorder. In this model, the layers are arranged in an ABC–CBA configuration. As shown in Fig. 5, we refer to the difference between the calculated total Chern number  $C$  from its theoretical value  $N - 2$  [36] to make the evolution clear, where  $N$  is the number of the layers. The random scattering disorder disturbs the linear relation between the number of layers and the total Chern number. The upper limit of 40 meV is critical because the flat band topology for twisted bilayer graphene essentially fails at this disorder strength [46]. The weak disorder that is smaller than the remote band gap will not affect the Chern number of the flat band at all. Additionally, the intervalley scattering could mix the Chern number from different bands. This could eventually cause the total Chern number to vanish. By adding the random scattering disorder and taking the statistical average of the total Chern number sequence, we conclude that the Chern number decreases with increasing the disorder amplitude.

In conclusion, we used the Zak phase to explain the emergence of the surface and interface states at twist stacking faults in rhombohedral graphite. The interplay between the moiré Brillouin zone dimensions and the Zak phase offers a physical framework for understanding the formation and evolution of surface and interface states. In the chiral limit, twisted rhombohedral graphite can host degenerate flat bands originating from both surface and interface states. Introducing non-chiral terms, such as the finite AA coupling, we split the degenerate bands and separate the surface and interface states.

The Chern number of the flat bands of the twisted rhombohedral graphite system is tunable with finite disorder at the surface. As the disorder increases, the Chern number gradually decreases and eventually vanishes, reflecting the breakdown of topological protection. This behavior highlights both the limitations and tunability of flat-band topology, and suggests a promising platform for exploring the interplay between localization, electronic correlations, and topological phases.

We thank Jianpeng Liu and Yaroslav Zhumagulov for the fruitful discussions. We acknowledge support by the Swiss National Science Foundation (grant No.204254). Computations were performed at the facilities of the Scientific IT and Application Support Center of EPFL.

\* [oleg.yazyev@epfl.ch](mailto:oleg.yazyev@epfl.ch)

- [1] R. Bistritzer and A. H. MacDonald, Moiré bands in twisted double-layer graphene, *Proceedings of the National Academy of Sciences* **108**, 12233 (2011).
- [2] S. Carr, D. Massatt, S. Fang, P. Cazeaux, M. Luskin, and E. Kaxiras, Twistrionics: Manipulating the electronic properties of two-dimensional layered structures through their twist angle, *Phys. Rev. B* **95**, 075420 (2017).
- [3] A. H. Castro Neto, F. Guinea, N. M. R. Peres, K. S. Novoselov, and A. K. Geim, The electronic properties of graphene, *Rev. Mod. Phys.* **81**, 109 (2009).
- [4] S. Das Sarma, S. Adam, E. H. Hwang, and E. Rossi, Electronic transport in two-dimensional graphene, *Rev. Mod. Phys.* **83**, 407 (2011).
- [5] Y. Cao, V. Fatemi, A. Demir, S. Fang, S. L. Tomarken, J. Y. Luo, J. D. Sanchez-Yamagishi, K. Watanabe, T. Taniguchi, E. Kaxiras, *et al.*, Correlated insulator behaviour at half-filling in magic-angle graphene superlattices, *Nature* **556**, 80 (2018).
- [6] A. L. Sharpe, E. J. Fox, A. W. Barnard, J. Finney, K. Watanabe, T. Taniguchi, M. A. Kastner, and D. Goldhaber-Gordon, Emergent ferromagnetism near three-quarters filling in twisted bilayer graphene, *Science* **365**, 605 (2019).
- [7] Y. Choi, J. Kemmer, Y. Peng, A. Thomson, H. Arora, R. Poliski, Y. Zhang, H. Ren, J. Alicea, G. Refael, *et al.*, Imaging electronic correlations in twisted bilayer graphene near the magic angle, arXiv preprint arXiv:1901.02997 (2019).
- [8] E. Codecido, Q. Wang, R. Koester, S. Che, H. Tian, R. Lv, S. Tran, K. Watanabe, T. Taniguchi, F. Zhang, M. Bockrath, and C. N. Lau, Correlated insulating and superconducting states in twisted bilayer graphene below the magic angle, *Science Advances* **5**, 10.1126/sciadv.aaw9770 (2019).
- [9] Y. Cao, V. Fatemi, S. Fang, K. Watanabe, T. Taniguchi, E. Kaxiras, and P. Jarillo-Herrero, Unconventional superconductivity in magic-angle graphene superlattices, *Nature* **556**, 43 (2018).
- [10] M. Yankowitz, S. Chen, H. Polshyn, Y. Zhang, K. Watanabe, T. Taniguchi, D. Graf, A. F. Young, and C. R. Dean, Tuning superconductivity in twisted bilayer

graphene, *Science* **363**, 1059 (2019).

[11] Z. Song, Z. Wang, W. Shi, G. Li, C. Fang, and B. A. Bernevig, All magic angles in twisted bilayer graphene are topological, *Phys. Rev. Lett.* **123**, 036401 (2019).

[12] J. Liu, J. Liu, and X. Dai, Pseudo landau level representation of twisted bilayer graphene: Band topology and implications on the correlated insulating phase, *Phys. Rev. B* **99**, 155415 (2019).

[13] J. Ahn, S. Park, and B.-J. Yang, Failure of nielsen-ninomiya theorem and fragile topology in two-dimensional systems with space-time inversion symmetry: Application to twisted bilayer graphene at magic angle, *Phys. Rev. X* **9**, 021013 (2019).

[14] C. Shen, Y. Chu, Q. Wu, N. Li, S. Wang, Y. Zhao, J. Tang, J. Liu, J. Tian, K. Watanabe, T. Taniguchi, R. Yang, Z. Y. Meng, D. Shi, O. V. Yazyev, and G. Zhang, Correlated states in twisted double bilayer graphene, *Nature Physics* **16**, 520 (2020).

[15] X. Liu, Z. Hao, E. Khalaf, J. Y. Lee, Y. Ronen, H. Yoo, D. Haei Najafabadi, K. Watanabe, T. Taniguchi, A. Vishwanath, and P. Kim, Tunable spin-polarized correlated states in twisted double bilayer graphene, *Nature* **583**, 221 (2020).

[16] Y. Cao, D. Rodan-Legrain, O. Rubies-Bigorda, J. M. Park, K. Watanabe, T. Taniguchi, and P. Jarillo-Herrero, Tunable correlated states and spin-polarized phases in twisted bilayer–bilayer graphene, *Nature* **10.1038/s41586-020-2260-6** (2020).

[17] G. Chen, L. Jiang, S. Wu, B. Lyu, H. Li, B. L. Chittari, K. Watanabe, T. Taniguchi, Z. Shi, J. Jung, Y. Zhang, and F. Wang, Evidence of a gate-tunable mott insulator in a trilayer graphene moiré superlattice, *Nat. Phys.* **15**, 237 (2019).

[18] G. Chen, A. L. Sharpe, P. Gallagher, I. T. Rosen, E. J. Fox, L. Jiang, B. Lyu, H. Li, K. Watanabe, T. Taniguchi, J. Jung, Z. Shi, D. Goldhaber-Gordon, Y. Zhang, and F. Wang, Signatures of tunable superconductivity in a trilayer graphene moiré superlattice, *Nature* **572**, 215 (2019).

[19] G. Chen, A. L. Sharpe, E. J. Fox, Y.-H. Zhang, S. Wang, L. Jiang, B. Lyu, H. Li, K. Watanabe, T. Taniguchi, *et al.*, Tunable correlated chern insulator and ferromagnetism in a moiré superlattice, *Nature* **579**, 56 (2020).

[20] Y. Shi, S. Xu, Y. Yang, S. Slizovskiy, S. V. Morozov, S.-K. Son, S. Ozdemir, C. Mullan, J. Barrier, J. Yin, A. I. Berdyugin, B. A. Piot, T. Taniguchi, K. Watanabe, V. I. Fal'ko, K. S. Novoselov, A. K. Geim, and A. Mishchenko, Electronic phase separation in multilayer rhombohedral graphite, *Nature* **584**, 210 (2020).

[21] T. Han, Z. Lu, G. Scuri, J. Sung, J. Wang, T. Han, K. Watanabe, T. Taniguchi, L. Fu, H. Park, and L. Ju, Orbital multiferroicity in pentalayer rhombohedral graphene, *Nature* **623**, 41 (2023).

[22] W. Zhou, J. Ding, J. Hua, L. Zhang, K. Watanabe, T. Taniguchi, W. Zhu, and S. Xu, Layer-polarized ferromagnetism in rhombohedral multilayer graphene, *Nature Communications* **15**, 2597 (2024).

[23] R. Guerrero-Avilés, M. Pelc, F. R. Geisenhof, R. T. Weitz, and A. Ayuela, Rhombohedral trilayer graphene is more stable than its bernal counterpart, *Nanoscale* **14**, 16295 (2022).

[24] H. Zhou, T. Xie, T. Taniguchi, K. Watanabe, and A. F. Young, Superconductivity in rhombohedral trilayer graphene, *Nature* **598**, 434 (2021).

[25] P. A. Pantaleón, A. Jimeno-Pozo, H. Sainz-Cruz, V. T. Phong, T. Cea, and F. Guinea, Superconductivity and correlated phases in non-twisted bilayer and trilayer graphene, *Nature Reviews Physics* **5**, 304 (2023).

[26] H. Zhou, T. Xie, A. Ghazaryan, T. Holder, J. R. Ehrets, E. M. Spanton, T. Taniguchi, K. Watanabe, E. Berg, M. Serbyn, and A. F. Young, Half- and quarter-metals in rhombohedral trilayer graphene, *Nature* **598**, 429 (2021).

[27] X. Zan, X. Guo, A. Deng, Z. Huang, L. Liu, F. Wu, Y. Yuan, J. Zhao, Y. Peng, L. Li, Y. Zhang, X. Li, J. Zhu, J. Dong, D. Shi, W. Yang, X. Yang, Z. Shi, L. Du, Q. Dai, and G. Zhang, Electron/infrared-phonon coupling in abc trilayer graphene, *Nature Communications* **15**, 10.1038/s41467-024-46129-7 (2024).

[28] Z.-Q. Jiao, S. Longhi, X.-W. Wang, J. Gao, W.-H. Zhou, Y. Wang, Y.-X. Fu, L. Wang, R.-J. Ren, L.-F. Qiao, *et al.*, Experimentally detecting quantized zak phases without chiral symmetry in photonic lattices, *Physical Review Letters* **127**, 147401 (2021).

[29] C.-K. Chiu, J. C. Teo, A. P. Schnyder, and S. Ryu, Classification of topological quantum matter with symmetries, *Reviews of Modern Physics* **88**, 035005 (2016).

[30] J. Zak, Berry's phase for energy bands in solids, *Phys. Rev. Lett.* **62**, 2747 (1989).

[31] A. Garcia-Ruiz, S. Slizovskiy, and V. I. Fal'ko, Flat bands for electrons in rhombohedral graphene multilayers with a twin boundary, *Advanced Materials Interfaces* **10**, 2202221 (2023).

[32] T. Kawakami, T. Nomura, and M. Koshino, Electronic properties of a graphyne-*n* monolayer and its multilayer: Even-odd effect and topological nodal line semimetallic phases, *Phys. Rev. B* **102**, 115421 (2020).

[33] R. Haering, Band structure of rhombohedral graphite, *Canadian Journal of Physics* **36**, 352 (1958).

[34] C. Fang, Y. Chen, H.-Y. Kee, and L. Fu, Topological nodal line semimetals with and without spin-orbital coupling, *Phys. Rev. B* **92**, 081201 (2015).

[35] A. Lau, T. Hyart, C. Autieri, A. Chen, and D. I. Pikulin, Designing three-dimensional flat bands in nodal-line semimetals, *Phys. Rev. X* **11**, 031017 (2021).

[36] J. Liu, Z. Ma, J. Gao, and X. Dai, Quantum valley hall effect, orbital magnetism, and anomalous hall effect in twisted multilayer graphene systems, *Phys. Rev. X* **9**, 031021 (2019).

[37] T. Han, Z. Lu, G. Scuri, J. Sung, J. Wang, T. Han, K. Watanabe, T. Taniguchi, L. Fu, H. Park, *et al.*, Orbital multiferroicity in pentalayer rhombohedral graphene, *Nature* **623**, 41 (2023).

[38] J. C. Slater and G. F. Koster, Simplified lcao method for the periodic potential problem, *Phys. Rev.* **94**, 1498 (1954).

[39] A. P. Thompson, H. M. Aktulga, R. Berger, D. S. Bolintineanu, W. M. Brown, P. S. Crozier, P. J. in 't Veld, A. Kohlmeyer, S. G. Moore, T. D. Nguyen, R. Shan, M. J. Stevens, J. Tranchida, C. Trott, and S. J. Plimpton, LAMMPS - a flexible simulation tool for particle-based materials modeling at the atomic, meso, and continuum scales, *Comp. Phys. Comm.* **271**, 108171 (2022).

[40] A. N. Kolmogorov and V. H. Crespi, Registry-dependent interlayer potential for graphitic systems, *Phys. Rev. B* **71**, 235415 (2005).

[41] D. W. Brenner, O. A. Shenderova, J. A. Harrison,

S. J. Stuart, B. Ni, and S. B. Sinnott, A second-generation reactive empirical bondorder (rebo) potential energy expression for hydrocarbons, *Journal of Physics: Condensed Matter* **14**, 783 (2002).

[42] Y. Xie, B. Lian, B. Jäck, X. Liu, C.-L. Chiu, K. Watanabe, T. Taniguchi, B. A. Bernevig, and A. Yazdani, Spectroscopic signatures of many-body correlations in magic-angle twisted bilayer graphene, *Nature* **572**, 101 (2019).

[43] P. J. Ledwith, A. Vishwanath, and E. Khalaif, Family of ideal chern flatbands with arbitrary chern number in chiral twisted graphene multilayers, *Physical Review Letters* **128**, 176404 (2022).

[44] H. Min and A. H. MacDonald, Chiral decomposition in the electronic structure of graphene multilayers, *Phys. Rev. B* **77**, 155416 (2008).

[45] S. Slizovskiy, E. McCann, M. Koshino, and V. I. Fal'ko, Films of rhombohedral graphite as two-dimensional topological semimetals, *Communications physics* **2**, 164 (2019).

[46] Y. Zhang, K. Jiang, Z. Wang, and F. Zhang, Correlated insulating phases of twisted bilayer graphene at commensurate filling fractions: A hartree-fock study, *Phys. Rev. B* **102**, 035136 (2020).

[47] S. Reich, J. Maultzsch, C. Thomsen, and P. Ordejón, Tight-binding description of graphene, *Phys. Rev. B* **66**, 035412 (2002).

[48] J. Herzog-Arbeitman, Y. Wang, J. Liu, P. M. Tam, Z. Qi, Y. Jia, D. K. Efetov, O. Vafek, N. Regnault, H. Weng, Q. Wu, B. A. Bernevig, and J. Yu, Moiré fractional chern insulators. ii. first-principles calculations and continuum models of rhombohedral graphene superlattices, *Phys. Rev. B* **109**, 205122 (2024).

# Supplementary Information of “Electronic states at twist stacking faults in rhombohedral graphite”

## CONTENTS

References	5
I. Methods	i
II. Band structure and bandwidth evolution from continuum model	ii
III. Band structure from tight-binding Green’s function	iii

## I. METHODS

The Hamiltonian of the tight-binding model is

$$\hat{H} = \sum_{i,j} t_\pi^{ij} c_i^\dagger c_j + \sum_{i,j} t_\sigma^{ij} c_i^\dagger c_j. \quad (\text{S1})$$

Explicit expressions for the hopping parameters  $t_\pi^{ij}$  and  $t_\sigma^{ij}$  are

$$\begin{aligned} t_\pi^{ij} &= V_\pi^0 \exp\left(-\frac{r - a_0}{r_0}\right), \\ t_\sigma^{ij} &= V_\sigma^0 \exp\left(-\frac{r - d_0}{r_0}\right). \end{aligned} \quad (\text{S2})$$

Following the previous Slater-Koster parametrization, we set  $V_\pi^0 = -2.7$  eV,  $V_\sigma^0 = 0.48$  eV [47], characteristic distances  $a = 2.46\text{\AA}$ ,  $a_0 = 1.42\text{\AA}$ ,  $d_0 = 3.35\text{\AA}$  and the decay length  $r_0 = 0.184a$ .

The continuum model of twisted rhombohedral graphene is built starting from the effective model for the multi-layer rhombohedral graphene. We focus on the low-energy states near the  $K$  point, which we refer to as the  $K$  valley, for multi-layer rhombohedral graphene, resulting in a  $2n \times 2n$  Hamiltonian whose basis is the layer inner product with the sublattice [48]. Expanding in the  $K$  valley, one obtains

$$H_{RG}(\mathbf{K} + \mathbf{k}) = \begin{pmatrix} v_F \mathbf{k} \cdot \sigma & t^\dagger(\mathbf{k}) \\ t(\mathbf{k}) & \ddots & t^\dagger(\mathbf{k}) \\ & t(\mathbf{k}) & v_F \mathbf{k} \cdot \sigma \end{pmatrix}, \quad (\text{S3})$$

$$t(\mathbf{k}) = \begin{pmatrix} -v_4 k & t_1 \\ -v_3 \bar{k} & -v_4 k \end{pmatrix}, \quad k, \bar{k} = k_x \pm i k_y. \quad (\text{S4})$$

In this Hamiltonian, the terms  $v_3$  and  $v_4$  used to represent trigonal warping and particle-hole asymmetry are neglected. The effect of the twist is described by the coupling  $T_\theta(\mathbf{r})$ , which gives

$$T_\theta(\mathbf{r}) = \sum T_n e^{-i\mathbf{q}_n \cdot \mathbf{r}} \quad (\text{S5})$$

with a moiré three-fold star  $\mathbf{q}_i = 2k_D \sin(\theta/2)$  equirotated by  $\phi = 2\pi/3$  and

$$T_n = e^{-i\mathcal{G}_\theta^{(n)} \mathbf{d}} \hat{\Omega}_\phi^{n-1} \begin{pmatrix} w_{AA} & w_{AB} \\ w_{AB} & w_{AA} \end{pmatrix} \hat{\Omega}_\phi^{1-n} \quad (\text{S6})$$

with  $\hat{\Omega}_\phi = \cos \phi \sigma_x - \sin \phi \sigma_y$ . Here,  $\mathcal{G}_\theta^{(0)} = 0$ ,  $\mathcal{G}_\theta^{(1)} = \mathbf{q}_2 - \mathbf{q}_1$ ,  $\mathcal{G}_\theta^{(2)} = \mathbf{q}_3 - \mathbf{q}_1$  are the moiré reciprocal lattice vectors and  $\mathbf{d}$  is the interlayer displacement [1]. The TRG Hamiltonian thus reads

$$H_{TRG} = \begin{pmatrix} v_F \mathbf{k} \cdot \sigma & t^\dagger(\mathbf{k}) & & & \\ t(\mathbf{k}) & \ddots & t^\dagger(\mathbf{k}) & & \\ & t(\mathbf{k}) & v_F \mathbf{k} \cdot \sigma & T_\theta^\dagger(\mathbf{r}) & \\ & & T_\theta(\mathbf{r}) & v_F \mathbf{k} \cdot \sigma & t^\dagger(\mathbf{k}) \\ & & & t(\mathbf{k}) & \ddots & t^\dagger(\mathbf{k}) \\ & & & t(\mathbf{k}) & v_F \mathbf{k} \cdot \sigma & \end{pmatrix} \quad (S7)$$

Another way to build the twisted rhombohedral graphene is via

$$H_{TRG} = \begin{pmatrix} H_{TBG} & H_{int} \\ H_{int} & H_{NLG} \end{pmatrix}. \quad (S8)$$

Here, the TBG block is constructed in the same way as described above, and the  $N$ -layer graphene block is based on the  $n$ -th order perturbation theory [44]

$$H_{NLG}^n = -t_\perp \begin{pmatrix} 0 & (v_F/t_\perp \mathbf{k}_M e^{i(\phi-\theta)})^n \\ (v_F/t_\perp \mathbf{k}_M e^{-i(\phi-\theta)})^n & 0 \end{pmatrix} + \eta \sigma_z, \quad (S9)$$

where  $\mathbf{k}_M = \sqrt{k_x^2 + k_y^2}$ ,  $\phi = \arg(k_x + ik_y)$ ,  $\theta$  is the twist angle,  $\eta$  is a small finite mass. It is necessary to mention, this model highly relies on  $t_\perp$ , so it only validates around the chiral limit.

## II. BAND STRUCTURE AND BANDWIDTH EVOLUTION FROM CONTINUUM MODEL

As shown in Fig. S1(a), the signature of the critical twist angle at  $\theta \approx 2.6^\circ$  is not sharply resolved in the total DOS. At this angle, the Zak phase in momentum space takes the value of  $\pi$  begins to approach the Brillouin zone center, and the flat bands at the  $\Gamma$  point gradually become dispersive. Notably, before reaching this critical angle, the Zak phase in momentum space takes the value of  $\pi$  has already started to overlap at the  $M$  point. At the critical angle, the bandwidth is approximately 20 meV. This energy scale is well-suited for exploring strongly correlated topological phases, where interaction effects are expected to dominate. More generally, when finite AA coupling is included, electrons tend to delocalize, whereas in the chiral-limit case, see Fig. S1(b), the bands collapse into highly degenerate, nearly perfectly flat bands.

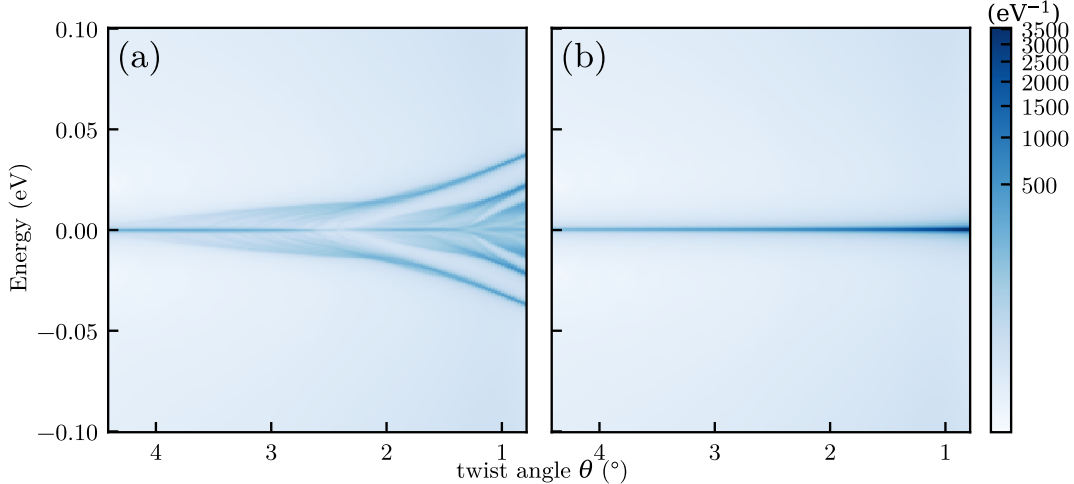


FIG. S1. The density of state (DOS) of twisted rhombohedral graphite as a function of  $\theta$ . (a) and (b),  $w_{AA} = 20$  meV and 0 meV, respectively.

In Fig. S2, we present the band structure of 8+8-layer twisted rhombohedral graphene to illustrate the distinction between the surface and interface states. The two types of boundary modes have different origins. The surface

states arise when the bulk is truncated by vacuum: the bulk–edge correspondence guarantees that the topological charge of the bulk phase must be discharged at the surface. In contrast, interface states appear at the domain boundaries between the regions characterized by different topological invariants: the mismatch enforces boundary-localized modes inside the bulk. In practice, the most reliable way to distinguish them is to compute their layer wavefunction localization.

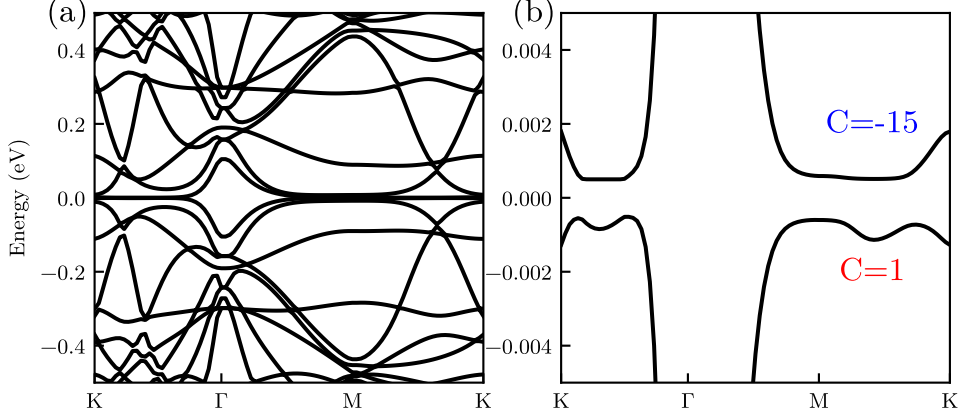


FIG. S2. (a) Electronic band structure of 8+8-layer twisted rhombohedral graphene in the ABC-CBA configuration obtained using the continuum model. (b) Same band structure plotted in a narrow energy range showing the surface and interface bands with their corresponding Chern numbers.

### III. BAND STRUCTURE FROM TIGHT-BINDING GREEN'S FUNCTION

The main difference between ABC-ABC and ABC-CBA configurations can be understood from the relaxation effect and the symmetry. From Fig. S3, we observe a clear contrast in the relaxation patterns between the ABC-CBA and ABC-ABC configurations. Here  $\Delta\mathbf{r}$  denotes the displacement between the unrelaxed and relaxed structures. The contrast clearly shows that the ABC-CBA stacking drives the middle TBG layers closer to the chiral limit, whereas ABC-ABC does not.

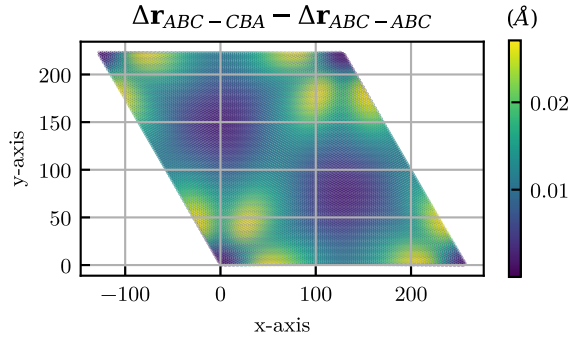


FIG. S3. The displacement difference between ABC-CBA and ABC-ABC configurations,  $\theta \approx 0.5^\circ$ .

From a symmetry perspective, we can understand this behavior from the untwisted case by using an effective Green's function,

$$G_{ABC-CBA} = \begin{pmatrix} 2\Sigma(E) & h(\mathbf{k}) \\ h^*(\mathbf{k}) & \end{pmatrix}^{-1}, \quad G_{ABC-ABC} = \begin{pmatrix} \Sigma(E) & h(\mathbf{k}) \\ h^*(\mathbf{k}) & \Sigma(E) \end{pmatrix}^{-1}, \quad (S10)$$

where  $\Sigma$  is the self-energy from the lead, and  $h(\mathbf{k}) = -t\phi(k_x, k_y) - \gamma_1 e^{ik_z c}$ . One can observe that the ABC-ABC configuration preserves the chiral symmetry with the energy shift. But for the ABC-CBA configuration, the self-energy is not equivalent for different sublattice sectors, which would provide a boundary mode without changing the bulk invariant. In this sense, the stacking fault would give us a flat band in rhombohedral graphite. When we introduce the twist stacking fault, this flat band would hybridize with the TBG flat bands, making the interface and surface flat bands flatten.

We compared the momentum resolved DOS from two different configurations but the same twist angle, as shown in Fig. S4, the ABC-CBA configuration produced better flat bands.

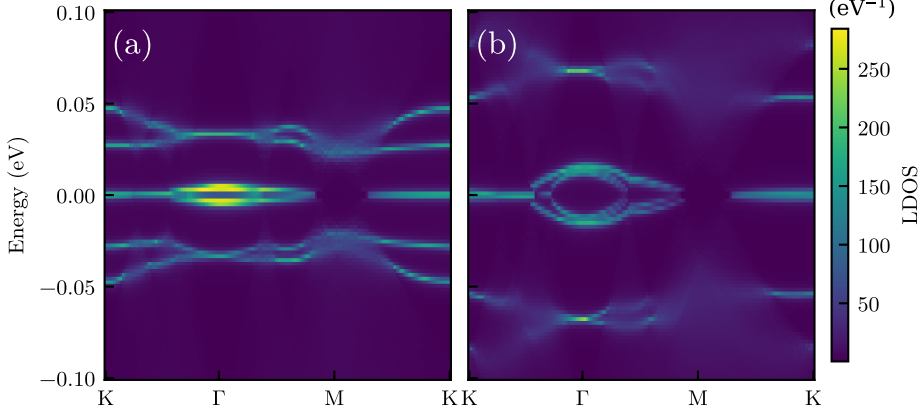


FIG. S4. Momentum resolved DOS, solved from Green's function, twist angle is  $2.13^\circ$ , (a) DOS for ABC-CBA configuration, (b) DOS for ABC-ABC configuration.

We also compute the 'magic angle' situation, as we showed in Fig. S5, the 'chiral limit' case has the isolated flat bands with almost zero dispersion.

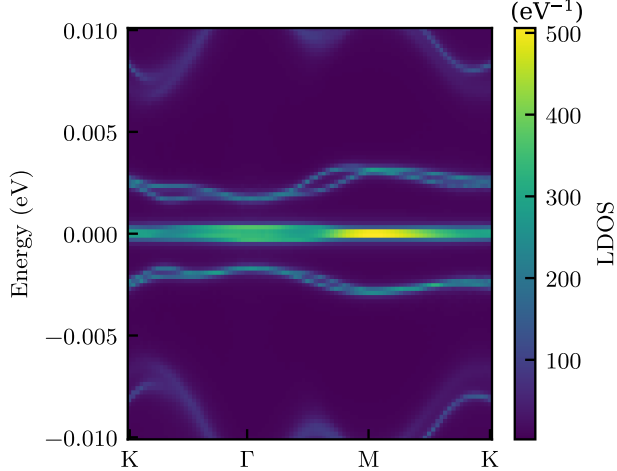


FIG. S5. Momentum resolved DOS, ABC-CBA configuration, the twist angle is  $1.08^\circ$ .